Whale Inspired Tubercles for Passively Enhancing the Performance of a Wind Turbine Blade

R Supreeth[*#‡], S K Maharana[**], Bhaskar K[#]

* Research Scholar, Department of Aeronautical Engineering, Acharya Institute of Technology, Bengaluru, India
# Faculty, Department of Aerospace Engineering, R V College of Engineering, Bengaluru, India

** Prof & Head, Department of Aeronautical Engineering, Acharya Institute of Technology, Bengaluru, India

(supreethr@rvce.edu.in, skmaha123@gmail.com, bhaskark@rvce.edu.in)

‡ Corresponding Author; R Supreeth, Department of Aerospace Engineering, R V College of Engineering, Bengaluru, India.

supreethr@rvce.edu.in

Received: 04.01.2022 Accepted: 28.01.2022

Abstract- In the underlying study, significant efforts are made to passively augment the performance of a *2kW* small scale horizontal wind turbine by implementing bioinspired humpback whale tubercles. Using blade element momentum theory, a baseline blade with smooth leading geometry was obtained. Subsequently, the tubercle with amplitude A_{LEP} =7% and wavelength λ_{LEP} =5% of the local chord c_i was interspersed to the leading edge of the baseline blade. Later, the performances of the baseline and modified blades were ascertained analytically, numerically, and experimentally at wind speeds U=1-20m/s and tip speeds $\lambda_{TR=}$1-20 respectively. The extensive investigation displays the tubercled blade to exhibit superior performance. Experimental outcomes demonstrated the tubercled blade to have an early cut-in at 3.26m/s against 3.71m/s of the baseline blade, which was a crucial factor for achieving sub-optimal operation and early power production. Additionally, the numerical results displayed the tubercled blade to exhibit higher torque Q, power P, and power coefficient C_P that were 14%, 17%, and 13% greater than the baseline blade.

Keywords: Leading Edge Tubercles, Passive Flow Control, Renewable Energy, Small Scale Wind Turbines, Wind Energy

1. Introduction

Share of electricity consumption is a straight forward indication of the human living standards dictated by GDP, per-capita income, life expectancy, literacy rate and many more [1]. Despite large scale global energy production, the per capita electrical consumption is not uniform across the globe. Lopsided energy production has severely hampered the socio-economic development of many people especially in the developing and under developed countries [2]. In fact, to date, nearly 840 million people globally have either extremely limited or absolutely no access to electric supply reflecting a poor growth index [3]. Research shows that the grave situation is not just linked to energy production, but also to the energy distribution mechanism as most people are found to reside in rural areas without power grid infrastructure [4]. Establishing new power grid stations require large infrastructure, huge labour force, periodic maintenance and many more that incurs monumental costs. Moreover, powering a small cluster of people located at different geographical locations is not an economically viable solution particularly for economically evolving nations.

In recent times, the small scale horizontal axis wind turbines (SSHAWT) are being developed as a last mile solution for portable power generation in remote areas, villages, small settlements, tribal localities, small buildings, etc [5][6]. They are no less important in big urban cities where small wind systems are beneficial in achieving self-sustenance and contributing to a greener environment. Although small scale wind turbines (SSWTs) are aggressively expanding, they do suffer from a few problems that affect their performance [7]. A Small scale wind turbine often needs to be implemented where the power is required and not necessarily where the wind resource is best [8]. The common installation locations of SSWTs are rooftops, buildings, small houses, farms, remote communities, streetlights, water pumping stations, remote military posts, etc [9] where it experiences severe atmospheric turbulence due to low hub height. Consequentially, the SSWTs are forced to operate at low Reynolds number, which is defined as the ratio of inertial forces to viscous forces. For

an airfoil, the Reynolds number is mathematically represented by Eqn. 1, where, ρ is the density of air in kg/m^3, U is the wind speed in m/s, c is the characteristic chord length of the airfoil in m, μ is the dynamic viscosity of air in N·s/m^2.

$$\mathrm{Re} = \frac{\rho U c}{\mu} \tag{1}$$

For SSWTs, small chord c and low wind velocities U will inevitably yield low Reynolds number mostly below *Re* =500000 along the entire span of the blade [10]. Flows in this regime possess shallow momentum that is unable to overcome strong pressure gradients on the blade leading to flow separation, high drag, low lift, stalling etc. Compared to the large-scale wind turbines (LSWTs), low *Re* number and lower wind speeds have pronounced effects on the performance of SSWTs that leads to low adaptability of SSWTs for power generation [11].

$$P = \frac{1}{2}\rho\pi R^2 U^3 C_p \eta \tag{2}$$

Furthermore, the power output for a wind turbine is represented by Eqn. 2 where P is the power output of the turbine in Watts, ρ is the density of the fluid in kg/m^3, R is the radius of the wind turbine in meters, U is the wind speed in m/s, C_P is the coefficient of performance of wind turbine, η is the generator efficiency. From the equation, P is proportional to the square of the radius R of wind turbine and cube of the wind velocity U. Wind turbines with small blade radius R operating at low wind speeds U, drastically reduces the power output P. Additionally, the frictional losses from generator shafts, bearings etc further reduce the power coefficient of the SSWTs to 0.20-0.30 as compared to 0.45-0.50 of LSWTs. Hence, at times, the power output of small wind turbines will generally be too low to even justify the construction and operational cost of the turbine [12] [13]. Power output can be enhanced by increasing the blade size and the operating height of the turbine. But doing this will unreasonably drive the installation and maintenance costs [14] and the very purpose of providing power to the needy at affordable costs will certainly die down. To overcome the apparent difficulties, new techniques and ideas are required to improve the efficiency of SSWTs cost effectively.

Identification of humpback whale tubercles as an excellent flow control device by Fish and Battle is a scientific breakthrough in the fluid dynamics community [15]. Humpback whales belong to the species of baleen whales and are popularly known for their large gigantic appearance. Humpbacks can grow up to 20m in length and weigh upwards of 40 tons. Despite their gigantic physical size, humpback whales are excellent swimmers with unmatched hydrodynamic maneuverability [16]. The extreme maneuverability of the humpbacks is attributed to the knob like structures on their flippers called the tubercles as shown in figure 1. From field observations by marine biologists, it was suggested that the tubercles act as passive flow control devices [17]. From hydrodynamic perspective, tubercles cause the flow to remain attached to the flipper over large angles of attack, thus delaying the flow separation. This eventually leads to higher hydrodynamic lift, enabling the whale to execute tight turns, roll, leap, break, breach, hunt at ease [18].

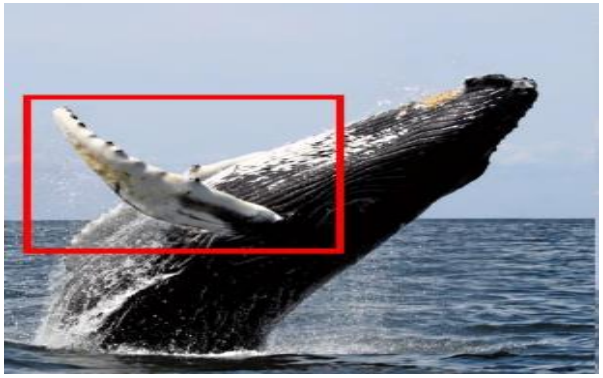

Fig. 1. Humpback whale flippers with tubercles [19]

To derive the benefits, several researchers have embraced the idea of tubercles to passively improvise the fluid dynamic characteristics. Using panel techniques, Watts et al [20] achieved higher lift (L) and lift-to-drag (L/D) of a tubercled wing by 4.8% and 17.6% respectively. Hansen et al [21] experimentally proved that the NACA 65-021 airfoil with tubercles had outstanding lifting characteristics as opposed to the airfoil without tubercles. Likewise, Ahmed Farouk Abdel Gawad [22] mimicked spherical tubercles for a NACA 0012 airfoil and numerically analysed its behavior for Re= 65000-1,000,000 through k-ε turbulence model in ANSYS. Simulation results manifested the tubercled to possess superior aerodynamic characteristics in terms of higher lift, delayed stall and better post stall performance. M C Keerthi et al [23] tested the contribution of leading edge tubercles for compressor blades with NACA 65209 blade profiles. The experimental outcomes showed the tubercles to be capable of suppressing blade stall and eventually improving the pre-stall range by at least by 43% as compared to the baseline compressor blade. Alok Mishra et al [24] numerically investigated the effect on transitional Reynolds number Re=120000 by the addition of tubercles for an airfoil. The study involving Delayed Detached Eddy Simulation (DDES) model which showed the spanwise flow over the modified airfoil interacts with the streamwise flow, thus delaying turbulent separation, and thereby expanding the stall and post stall behavior of the tubercled model. Benjamin Arrondeau et al [25] employed the k-ω *SST* turbulence model to study the effect of implementing tubercles on an F1 front-wing. A clear difference in aerodynamic performance was evident for the undulated wing, which produced more than 22% and 9% of lift L and L/D ratio across the tested range.

In an attempt to gain insight into the actual role of tubercles in enhancing flow characteristics, Rostamzadeh et al [26] employed Prandtl's nonlinear lifting-line theory to find the nature of circulation around the tubercled and non-tubercled wings and compared with numerical and experimental results. The outcomes evidently showed the tubercles to generate a pair of streamwise counter rotating vortices that were the primary reasons behind the boundary layer enhancement and improvement in the aerodynamic behavior. Further, Miklosovic [27] proposed that the leading edge tubercles are analogous to vortex generators that aid in amplifying the momentum exchange across the boundary layer.

Similarly, some authors have tried tubercles for wind turbine airfoils. Supreeth et al [28] attempted to quantify the aerodynamic improvisations contributed by tubercles to NREL S823 low Reynolds number airfoil, chiefly for horizontal axis wind turbine blades. The numerical and experimental results proved beyond any doubt that the S823 airfoil with tubercles extended overly good aerodynamic augmentation in terms of large lift and low drag across stall and post stall regimes. From experiments, Arunvinthan et al [29] found that irrespective of the tubercle dimension, the time-averaged lift coefficient surged for the tubercled blades. Comparably, Guo-Yuan Huang et al [30] inferred that by adding smaller amplitude tubercles to the wind turbine blades, the performance improved mainly in the stalling region. Chang-Chi Huang et al [31] indicated that by integrating the protuberances to the entire blade span, the performance of the small scale wind turbine was appreciably strengthened in comparison with the baseline blade. With particle image velocimetry, Weichao Shi et al [32] physically demonstrated the generation of extra torque on wind turbine blades with leading edge tubercles.

Though tubercles offered far-reaching aerodynamic benefits, it was mimicked majorly for untapered and untwisted blades. But for a wind turbine, twist and taper are characteristic features that cannot be neglected. Hence, the primary intent of the study is to evaluate the contribution of tubercles for blades with both spanwise taper and twist. To accomplish the objective, the blade element momentum theory (BEMT) would be employed for designing, scaling and analyzing the baseline blade for a *2kW* wind turbine at different flow conditions. Following, a tubercle geometry exhibiting suitable amplitude A_{LEP} and wavelength λ_{LEP} will be interspersed along the leading edge of the blade. Subsequently, the performances of the baseline and modified blades would be tested numerically and experimentally which will finally be compared with BEM values.

2. Wind Turbine Blade Design

Blade element momentum theory (BEMT) enumerated in [33] has been employed for designing, scaling and analyzing the performance of the baseline rotor blade. For the power rating, the design and operational specifications for the *2kW* scaled down wind turbine are given in table 1. Besides, the cross sectional profiles of the blade airfoils and their spanwise distribution can be comprehended from fig.2 and 3 respectively. Once the geometry of the blade is finalized, its performance would be estimated at wind velocities U=1-20m/s. Typical wind velocities experienced by large wind turbine would be between 3-25m/s [34]. But for a small scale wind turbine the operating wind velocities would anywhere be between 2-10m/s [35]. Hence, in the study, the wind turbine blades are tested for velocities 1-20m/s covering the maximum range of operation of both small and large scale wind turbines.

Table 1: Specifications of the *2kW* wind turbine

PARAMETERS	VALUE
Rated Power Output P_{Rated}	*2kW*
Wind Velocity Range U	1-20m/s
Inboard Airfoil (*0.05R-0.4R*)	NREL S823
Outboard Airfoil (*0.45R-1R*)	NREL S822
Design Tip Speed Ratio λ_{TSR}	7
Design Wind Speed U_{Design}	10m/s
Number of Blades B	3
Diameter of the Blade D	0.5m
Radius of the Blade R	0.22m
Hub Radius R_h	0.03m
Air Density ρ	1.23kg/m3
Generator Efficiency η_{Gen}	90%
Average Reynolds number *Re*	150000

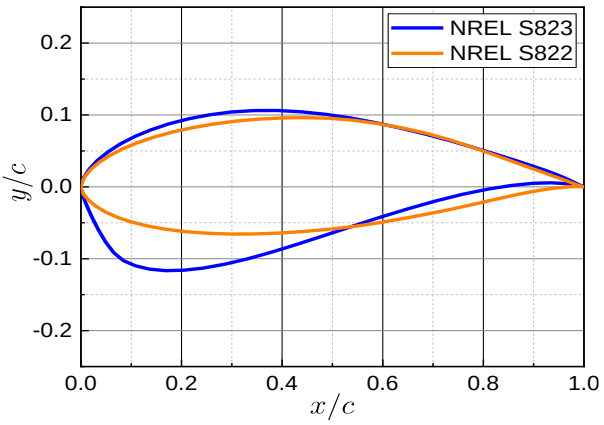

Fig. 2. Geometric profiles of NREL S823 and S822 airfoils

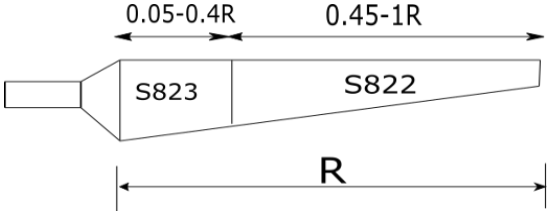

Fig. 3. Distribution of S823 and S822 airfoils along the span of the rotor blade

3. Numerical Methodology

3.1 Baseline and Modified Geometry

Based on the BEMT, the baseline and the modified blades obtained for the wind turbine modeled in CATIA are shown in figures 4a and 4b. The modified blade is generated by incorporating the tubercle of amplitude A_{LEP}=7% and wavelength λ_{LEP}=5% of the local chord c_i as displayed in figure 4c. The selection of tubercle geometry is in accordance with the optimum geometry proposed by Guo-Yuan Huang et al [30].

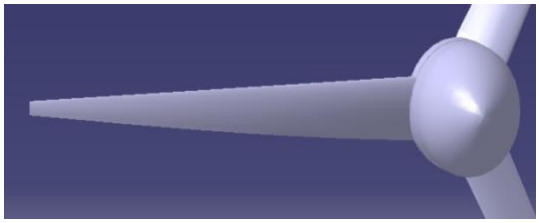

(a)

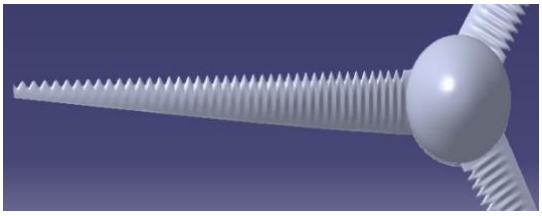

(b)

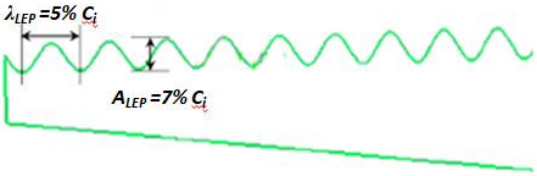

(c)

Fig. 4. Representation of the CAD models of the rotor blade a) Baseline blade b) Modified blade c) Depiction of amplitude A_{LEP} and wavelength λ_{LEP} geometry of the tubercle

3.2 Numerical Simulation

In the numerical simulation, the commercial software ANSYS FLUENT was utilized to estimate the performance of the wind turbine rotor blade for different upstream flow conditions. In order to simulate, just one rotor blade with the hub and nose cone dissected at 120° was considered. Firstly, the computational domain for the baseline and the modified blades were created. The front and the top portion of the fluid domain are demarcated as velocity inlet whereas the rear portion as pressure outlet. The remaining two sides are applied with the periodic boundary conditions. Inlet is at a distance of 10 times the root chord length of the blade to ensure the numerical perturbation does not influence the numerical solution at the blade. To ensure similar behavior, the distance of the outlet and the far-field are at distances 15 and 13 times the root chord length of the blade respectively. The fluid domain downstream to the blade is longer than the counterpart to capture the helical wake of the rotor blade. The details of the domain are shown in fig 5.

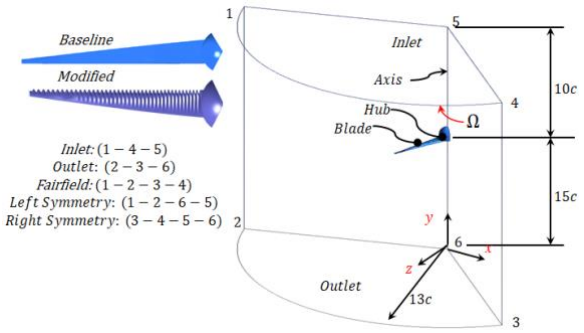

Fig. 5. Representation of dimensions of the domain

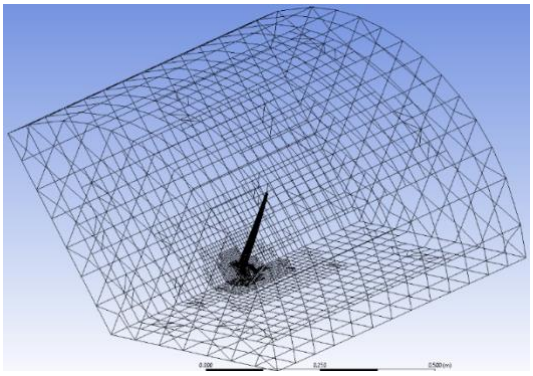

(a)

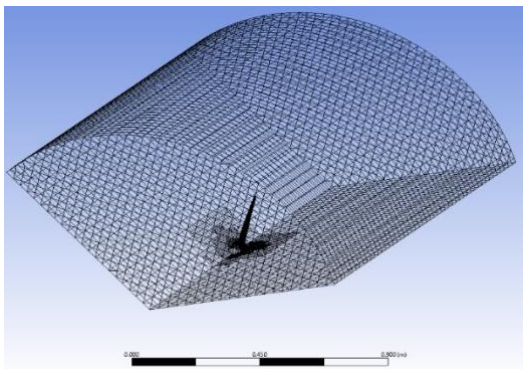

(b)

Fig. 6. Discretization of the domain a) Baseline blade b) Modified blade

Later, the computational domains were individually meshed using the cut-cell technique and the resulting grids are depicted in fig 6. In the cut-cell technique, the cells are cut rather than stretching and compressing to match the complex geometrical interfaces. The cut-cell technique renders the grid to fit perfectly to the domain geometry, thereby reducing the number of inaccuracies majorly caused by lack of skewness.

The greatest advantage of cut-cell method is its ability to handle complex moving geometries much more easily and accurately with added cell refinement at the wall [36].

Next, to precisely capture the flow behavior, the mesh was made finer at the blade surfaces and coarsened at regions away from the blade. Figure 7 manifests the nature of the grid distribution around the baseline blade and the modified blades. A closer look at the blade indicates the cell adaption along the blade-hub as well as hub-domain interfaces. To numerically simulate flows over the wind turbine blade, the time-averaged continuity and momentum equations for steady flow conditions given by equations 3 and 4 were utilized.

$$\frac{\partial U_i}{\partial x_i} = 0 \tag{3}$$

$$\rho\bar{u}_j\left(\frac{\partial \bar{u}_i}{\partial x_j}\right) = \frac{\partial \bar{p}}{\partial x_i} + \mu\frac{\partial}{\partial x_j}\left[\frac{\partial u_i}{\partial x_j} + \frac{\partial u_j}{\partial x_i}\right] - \frac{\partial}{\partial x_j}\left(\rho\overline{u_i' u_j'}\right) \tag{4}$$

In Eqn. 3, U_i is the average velocity vector in three dimensions. Similarly, in Eqn. 4, the total convective change in mean momentum is represented by the term on the left hand side of the equation, which is balanced by mean pressure field $\bar{p}$, stresses developed due to the viscous term $\mu\frac{\partial}{\partial x_j}\left[\frac{\partial \bar{u}_i}{\partial x_j} + \frac{\partial \bar{u}_j}{\partial x_i}\right]$ and the Reynolds stress represented by $\left(\rho\overline{u_i' u_j'}\right)$ is the mean turbulent velocity fluctuations. Here, ρ is the density (kg/m^3), μ is the fluid viscosity (N·s/m^2), $\overline{u_i'}$ and $\overline{u_j'}$ are the velocity fluctuation components (m/s), the subscripts i and j are the free indices with i and j =1,2,3 representing x,y and z directions respectively. The additional modelling to obtain the Reynolds stress term is satiated with the use of the *SST k-ω* model. The *SST k-ω* turbulence numerical model considers two additional transport equations i.e., the kinetic turbulent energy k and the specific turbulent dissipation rate ω as given by equations 5 and 6 respectively.

$$\frac{\partial k}{\partial t} + u_j\left(\frac{\partial k}{\partial x_j}\right) = P_k - \beta^* k\omega + \frac{\partial}{\partial x_j}\left[\left(\nu + \sigma_{k1}\nu_T\right)\left(\frac{\partial k}{\partial x_j}\right)\right] \tag{5}$$

$$\frac{D\omega}{Dt} = \frac{\gamma_1}{\nu_T}\tau_{ij}\left(\frac{\partial u_i}{\partial x_j}\right) - \beta_1\omega^2 + \frac{\partial}{\partial x_j}\left[\left(\nu + \sigma_{\omega 1}\nu_T\right)\left(\frac{\partial \omega}{\partial x_j}\right)\right] \tag{6}$$

In equation 5, the turbulent kinematic eddy viscosity ν_T is represented by equation 7, in which $\Omega_{Strain\text{-}rate}$ is the shear strain rate, a_1 is a proportionality constant such that $\tau = a_1\rho k$ and k is the turbulent kinetic energy.

$$\nu_T = \frac{\mu_T}{\rho} = \frac{k}{\omega} = \frac{a_{1k}}{\max\left(a_{1\omega}, \Omega_{strain\text{-}rate}\right)} \tag{7}$$

The constants in equation 6 for the *SST k-ω* model are given below from equations 8 to 13.

$$\sigma_{k1} = 0.85 \tag{8}$$

$$\sigma_{\omega 1} = 0.5 \tag{9}$$

$$\beta_1 = 0.075 \tag{10}$$

$$\beta^* = 0.09 \tag{11}$$

$$k = 0.41 \tag{12}$$

$$\gamma_1 = \frac{\beta_1}{\beta^*} - \frac{\sigma_{\omega 1} k^2}{\sqrt{\beta^*}} \tag{13}$$

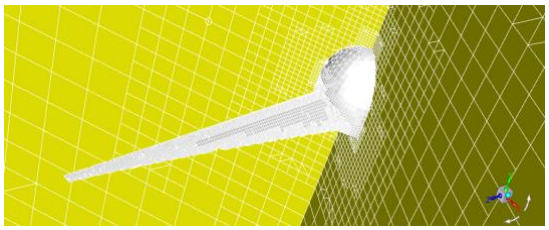

(a)

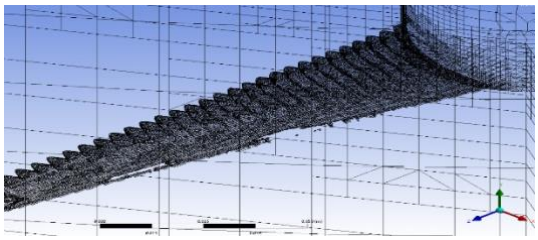

(b)

Fig. 7. Distribution of grid across the blade and the computational domain a) Baseline blade b) Modified blade

By using the second-order upwind and central difference schemes, the kinetic turbulent energy k and the specific turbulent dissipation rate ω are discretized. Further, the pressure velocity coupling is realized through the semi-implicit method for pressure-linked equations. Pressure Based Navier Stokes (PBNS) solver with *k-ω SST* model is considered to obtain information on aerodynamic forces, velocity streamlines, and torque generated on the blade while preserving the relaxation factor as 1 and 0.9 respectively. As wind turbine analysis is an initial boundary value problem, the simulation was initially run for a steady case before switching over to transient analysis. The convergence was monitored within a residue of 1e-5 with the time step size and the number of time steps set at 1e-5 and 5e5 for all the cases respectively. Turbulence intensity and turbulence viscosity ratio at inlet and outlet boundaries were noted to be 1% and 1 respectively.

Lastly, the domain wall and the solid boundaries were imposed with no-slip adiabatic conditions.

To analyze the performance of the wind turbine, the sliding mesh technique was preferred where the outer domain was defined stationary while the inner domain was rotating. The blade, blade tip and the hub were subjected to boundary conditions specified by free stream wind velocity U and angular velocity Ω of the blade. The torque Q generated by the blade for the given flow velocity was considered for estimating the blade performance. Once the boundary conditions were specified, the grid independence was performed to check the influence of cell size on the computational results and accuracy. The result of the grid independence study for baseline and the modified blade is provided in fig 8.

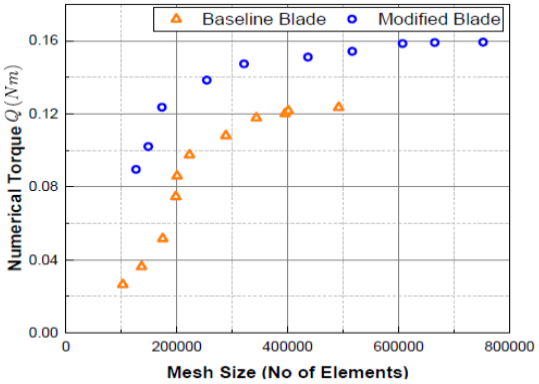

Fig.8. Grid independence for baseline and modified blades

4. Experimental Studies

4.1 Wind Turbine Embodiment

The wind turbine embodies many components like the blades, hub, nosecone, generator, nacelle, tower and baseplate. The baseline and modified blades, hub and nose cone were 3D printed with PETG material. Later, the blades were rendered a smooth surface finish using 5µm emery paper. The blades were designed with dovetail root that facilitated easy assembly and disassembly from the hub. The 3D printed baseline and modified blades are displayed in fig 9. The blade, hub and nosecone were keyed into the 5mm diameter shaft of the Swiss made Faulhaber minimotor PMDC producing 60W and 70mNm of rated power and torque. The nacelle with the blade assembly was then mounted on a 280mm vertical strut supported on a baseplate rigidly fixed to the wind tunnel floor. A tachometer with a range of up to 100,000rpm was fixed on the nacelle to measure the blade speed. A 360^0 angular protractor was necessary to maintain the alignment of the wind turbine to the flow. The complete wind turbine test rig assembly with all the critical components is given in fig 10. Complimentarily, the layout of the wind turbine test rig and associated instrumentation is illustrated in fig 11.

Fig. 9. 3D printed baseline and modified blades

(a)

(b)

Fig. 10. Wind turbine test rig a) Baseline b) Modified blades

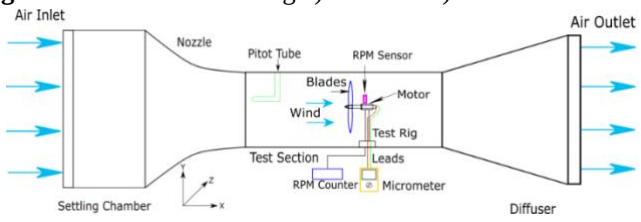

Fig.11. Schematic of the wind turbine test rig placed inside the open circuit wind tunnel test section

4.2 Wind Tunnel Calibration and Uncertainty Studies

Wind turbine testing was performed in a low speed open circuit wind tunnel. The wind tunnel is equipped with honeycombs, multi-level screens, and flow straighteners at the inlet to produce a smooth laminar flow with turbulence less than 1% in the 0.6m*0.6m*2m test section. Prior to testing, the tunnel was calibrated with the manufacturer's data which was found extremely matching. In addition, the uncertainties propagated during the experiments were also accounted as per Hugh et al [37]. The overall uncertainties occurring from tachometer, angular protractor, tunnel test section, electronic pressure manometer amounted to less than 2.5%.

Testing of the wind turbine performance began with the establishment of flow velocity in the tunnel test section. The flow velocity was constantly monitored by a pitot-static probe connected to an electronic pressure manometer. Originally, the experiment was planned for flow velocities 1 to 20m/s, but upwards of 10m/s, the blades experienced severe rotational speeds. Anticipating damages to the blades at high wind speeds, the experiment was forcefully stopped at 10m/s and the performance of the blades is reported only for velocities 1-10m/s. The power output of the wind turbine at different wind velocities was measured from Eq.14.

$$P = V * I \tag{14}$$

5. Results and Discussions

The succeeding section portrays the numerical and experimental responses of the wind turbine with baseline and modified blades and compares them with the BEM results. The graphical comparisons provide worthy insights about the blade behavior at the tested conditions.

5.1 Analytical, Numerical and Experimental Results

The torque Q of the rotor blade is treated as the evaluation parameter to directly derive the power output P and coefficient of power C_P. The numerical and experimental torque output Q of the baseline and the modified blades are presented in fig.12 alongside the BEM results. The numerical analysis was performed for wind velocity 2-20m/s for a consecutive step length of 2m/s and experimental testing was done only for velocity 1-10m/s. From the graphical comparison, the torque output of both the blades is found to parabolically rise with the wind velocity. The analytical and numerical values for the baseline blade are found to supremely coincide with each other in the entire range of tests. The coincidence is discerned up to 12m/s beyond which there is a deviation, though being very small. On the other hand, the modified blade too revealed a similar fashion but positively offset from the baseline values. This undoubtedly confirms the outstanding performance of the tubercled blade as noticed from the graph. The torque of the modified blade tested in ANSYS and experiment yielded similar values which were greater than the baseline model.

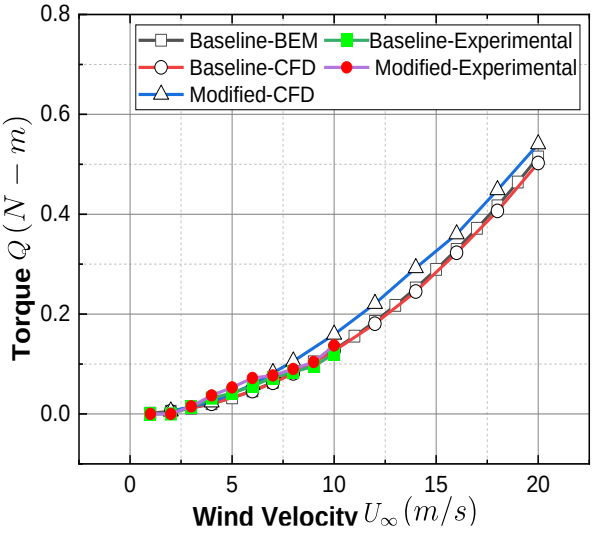

Fig.12. Comparison of the analytical, numerical and experimental torque Q of the baseline and modified blades

$$Q = I * K_Q \tag{15}$$

The experimental torque for the wind turbine blades was calculated using Eqn.15 where Q is the experimental torque in Nm, I is the experimental current in Ohms and k_Q is the torque constant for the Faulhaber minimotor. The numerical and experimental torque of the modified blade was coincidental up to 6m/s, beyond which the experimental torque somewhat dropped but restrained to be greater than the baseline torque. The numerical and experimental torque output for the modified blade at design velocity was computed to be 26% and 7% more than the BEM torque.

The analytical and numerical rotor power for the blades were ascertained through the Eq.16, where P_{Mech} is the mechanical power generated by the blade in Watts, Q is the rotor torque in Nm for three blades fetched through ANSYS and Ω is the angular velocity of the blade in rad/s corresponding to the upstream velocity. Contrastingly, the power output from a wind turbine generator will purely be in electrical format $P_{Electrical}$ which is quite contrary to the mechanical power P_{Mech} obtained from BEM and CFD techniques. In order to make a fair comparison, the power output of the generator should mandatorily be converted to a mechanical form. The methodology detailed by Bastankhah et al [38] has been applied to determine the mechanical power P_{Mech} and mechanical power coefficient C_{PMech} for the rotor blade. The power P and coefficient of power C_P thus obtained are compared with the analytical and numerical results in figures 18 and 19.

$$P_{Mech} = Q * \Omega \tag{16}$$

It can be noticed from the fig.13, the power P of the baseline blade from ANSYS begins with a small value. With an increase in the wind velocity, the power output escalates rather in a non-linear fashion corresponding to the torque trend. The numerical results of the rotor power output for the baseline model do not fluctuate much with the BEM power output as perceived from the figure. At design velocity, the numerical power output for the baseline rotor was 39.96W which is 1.69% less than the analytical power equivalent to 40.65W. At 20m/s, the difference between the ANSYS and BEM power was 2.3% which is still satisfactory. Considering the modified blade, the numerical power was distinctively superior to the baseline blade. The power developed by the modified blade was found to be 3.5% more at the initial velocity. Incrementing the velocity, the modified blade generated larger power output than the baseline blade. At U=10m/s, the modified blade generated 26% more power than the blade without tubercles. The power output for the modified blade increased non-linearly albeit with a higher power up to the last velocity the blade was tested for.

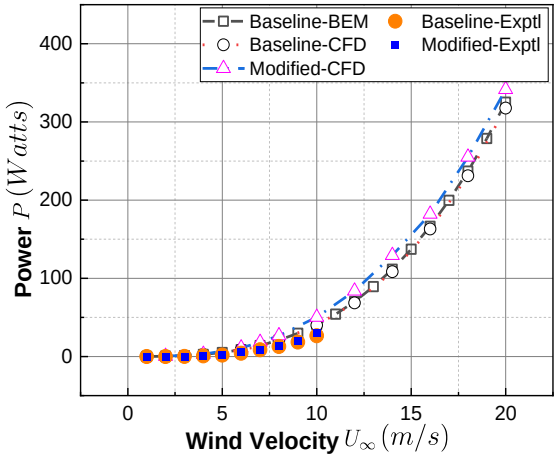

Fig.13. Power output P of the baseline and modified blades measured using BEM, CFD and Experimental techniques

Next, the experimental power for baseline and modified blades are compared with the BEM and CFD results in the same figure. As already highlighted, the experiment was conducted for velocities 1-10m/s, across which the behavior of the blades was found to be satisfactory. The experimental power output of the baseline and modified blades depicted a zero output at initial velocities but registered their first finite power only at 3.71m/s and 3.26m/s respectively as clearly manifested in the graph. Incrementing the wind speeds in the wind tunnel test section correspondingly surged the power output that began in a parabolic fashion. From the graph, it is seen that the power of the modified blade is fairly higher than the baseline blade across the range of testing. At the last velocity, the power output of the baseline and modified blades were 26.6W and 30.24W respectively.

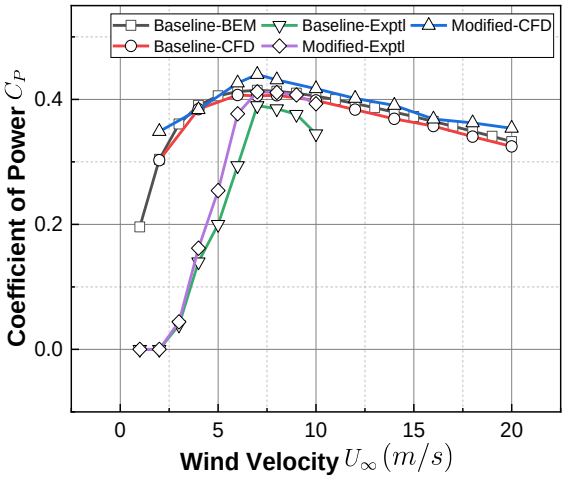

Fig.14. Coefficient of power C_P for the baseline and modified rotor blades

The coefficient of power C_P which is the figure of merit for any wind turbine determined analytically, numerically and experimentally is provided in fig 14. The coefficient of power for both the blades are analyzed based on the mechanical power output and is very much similar to any typical HAWT. The coefficient of power is analyzed for λ_{TSR} varying between 1-20 for the BEM case, 2-20 for the numerical and 1-10 for the experimental case. The analytical C_P for the baseline blade shoots from λ_{TSR}=1 itself and increases linearly till λ_{TSR}=3. But at λ_{TSR} =4, the BEM C_P registers a slight drift in linearity and proceeds in that direction till it reaches a maximum C_P at λ_{TSR} =7. Beyond λ_{TSR}=7, the C_P for the baseline blade diminishes and continued to fall steadily for the rest of the tip speeds.

Looking at the numerical C_P of the baseline blade, the curve gave away a trend similar to the analytical graph. The numerical C_P was recorded first at λ_{TSR}=2, and gradually increased with the tip speed. Throughout testing, the numerical C_P for the baseline blade closely followed the trend of the analytical C_P as seen in the figure. As the wind speeds increased, the C_P also gradually improved and attained a maximum C_P at λ_{TSR}=7. For both the BEM as well as the CFD cases, the baseline blade projected a maximum C_P of 0.414 and 0.409 independently at the design tip speed ratio. The percentage change in the CFD power coefficient was a meager 1% compared to the BEM value.

Considering the modified blade, the numerical C_P was incidentally greater than the baseline values. This was true for all the tip speeds. The graph clearly suggests the modified blade developed more power and hence a better coefficient of power than the baseline blade. The numerical C_P of the modified blade was 0.439 at design λ_{TSR}, which was around 6% and 9% more pronounced than the analytical and

numerical output for the baseline blade. Contrastingly, it can be noticed that the C_P curve for both the blades tested experimentally manifests faintly dissimilar curves albeit more realistic than the other two cases. In any real environment, it is almost impossible for a wind turbine to develop any minimum power for wind speeds below 3m/s. Owing to this, the experimental C_P plot for both baseline and modified blades recorded zero C_P at for wind velocities U=1m/s and 2m/s. Contrarily, the BEM theory and numerical simulations predicted positive C_P even at U=1, 2 and 3m/s respectively. Although the experimental C_P for the baseline and modified blades were zero at the initial two TSRs, it indeed started to rise for tip speeds beyond λ_{TSR}=3. The baseline and modified blades registered their first break of finite mechanical power at 3.71m/s and 3:26m/s. The C_P at these particular TSRs for the baseline and modified blades is of great significance as it recognizes the cut-in or start-up velocity for any wind turbine blade. It can be noticed that the tubercled blade displayed a start-up velocity much earlier than the baseline blade. Surging the TSR ahead, the C_P output of the baseline and modified blades incremented linearly, although the modified blade was prominently higher as seen in the figure. When the TSR approached the design condition, the baseline and modified blades registered maximum C_P=0.39 and 0.412 respectively which was 7% higher than the baseline blade, but less than the analytical or numerical value at the same tip speed. Post λ_{TSR}=7, the experimental C_P for the blades declined drastically against a more gradual nature of the BEM and numerical results as noticed from the graph.

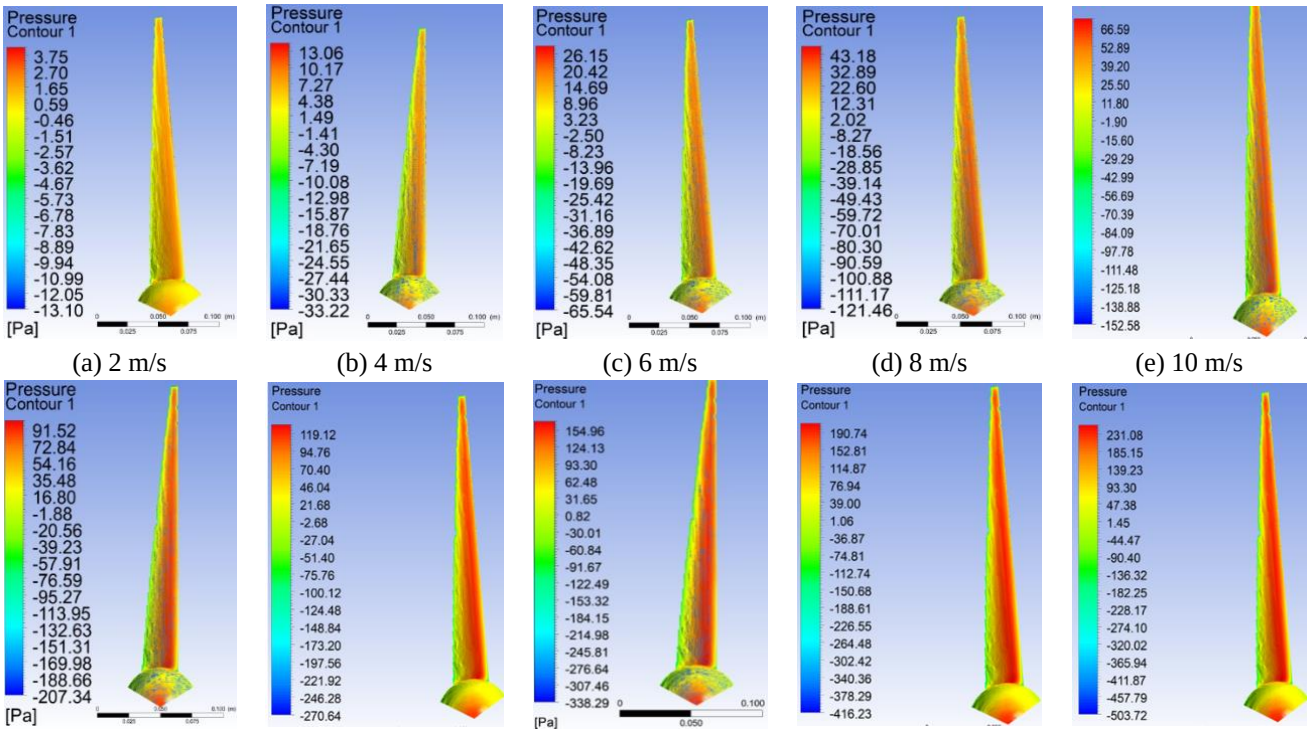

(a) 2 m/s (b) 4 m/s (c) 6 m/s (d) 8 m/s (e) 10 m/s

(f) 12 m/s (g) 14 m/s (h) 16 m/s (i) 18 m/s (j) 20 m/s

Fig.15. Pressure contours over the suction side of the baseline blade for 1-20m/s wind velocities

The pressure and velocity distribution over the baseline and modified blades at different wind velocities are displayed in fig 15 to fig 18. At the outset, the pressure contours over the blade surfaces in fig 15 look similar at all the velocities. Yet, closer examination divulges quantitative information on the pressure distribution over the blade surfaces. Firstly, it is discovered that the blade displays a gradient pressure distribution over the blade surfaces. At 2m/s, the maximum pressure noticed on the suction side of the blade was 3.75Pa, which then improves with the wind velocity. Contrastingly, even negative pressures are noticed on the blade surface that was tending to change with the surge in flow velocity. At design velocity, the highest pressure on the upper surface was 66.69Pa that ultimately attained 231.08Pa at 20m/s. From the figure, the highest pressure occurs along the leading edge and lessens slowly at the trailing edge. In fact, the least pressures noticed are at the trailing edge of the blade. The visual comparison between the pressure contours of the baseline and modified blades highlights a stark difference in pressure distribution over the suction side of the blade. In fig 16, starting at U=2m/s, the pressure difference over the suction side of the tubercled blade is found to experience a greater pressure gradient along the entire span of the blade. The minimum and maximum pressures experienced by the tubercled blade at 2m/s were 25.25Pa and 8.44Pa. The same nature in the pressure distribution can be viewed at all the other velocities. In fact, the difference in the pressure

differences tends to widen for the tubercled blade with incremental velocities.

Likewise, the velocity vector over the modified blade is given in fig 18. The velocity vector plots too are informative about the positive benefits demonstrated by the tubercled blade. From the figure, the velocity distribution for the modified blade is pronouncedly more than the baseline blade at all the velocities as shown in fig 17. For instance, at *U*=2m/s, the baseline blade produced a maximum tip velocity of 13.75m/s whereas the tubercled blade had a maximum tip velocity of 15.54m/s. This suggests that for a given velocity, the modified blade is rotating quite faster than the baseline blade. The trend appears to be similar at other velocities too. At the design velocity, the tubercled blade projected a velocity equivalent to 77.72m/s in comparison to 74.27m/s of the baseline blade. The modified blade velocities were notably increasing with the incoming wind as perceived from the figure. When the wind was 20m/s, the tip velocity for the modified blade measured 155.43m/s against 143.04m/s of the baseline blade.

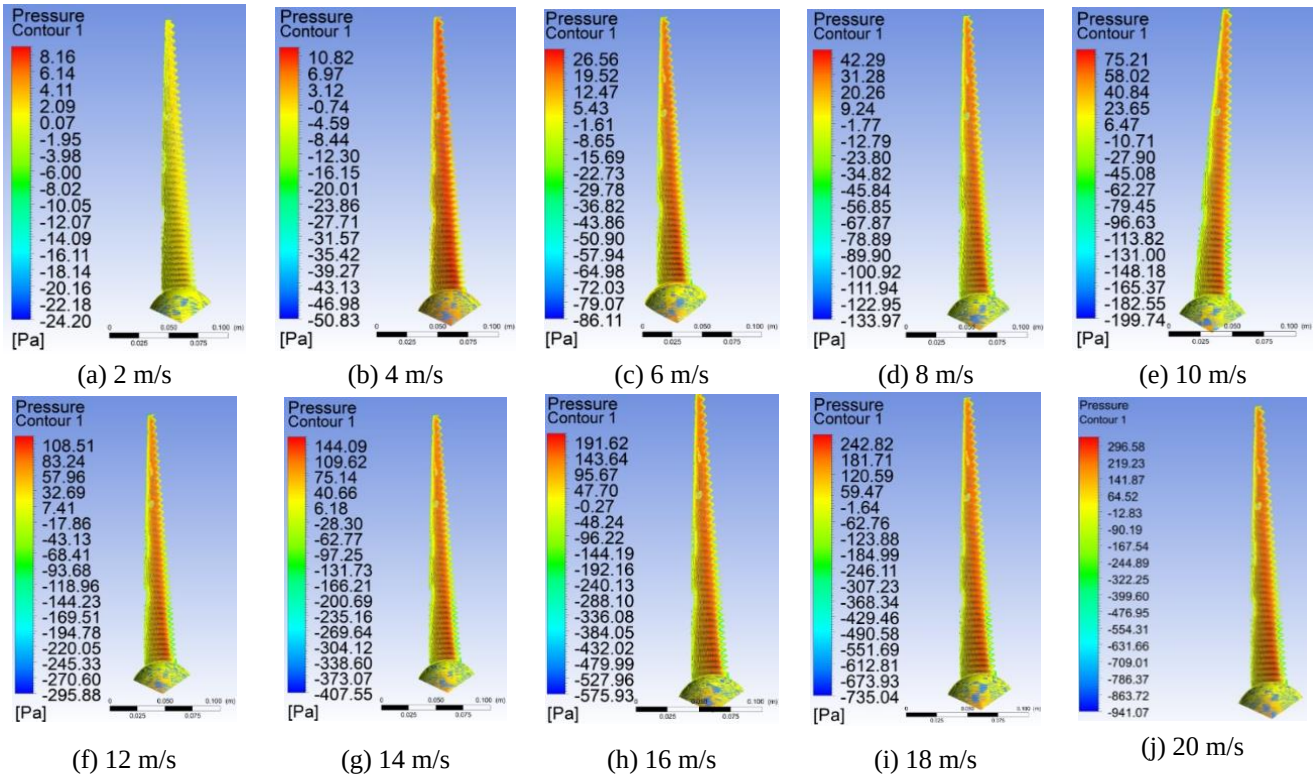

(a) 2 m/s (b) 4 m/s (c) 6 m/s (d) 8 m/s (e) 10 m/s

(f) 12 m/s (g) 14 m/s (h) 16 m/s (i) 18 m/s (j) 20 m/s

Fig.16. Pressure distribution over the suction side of the modified blade at different wind velocities tested numerically

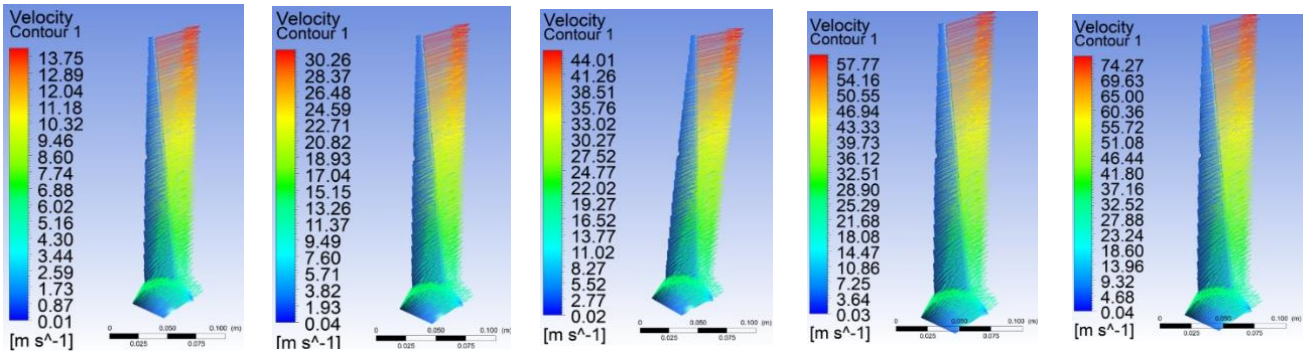

(a) 2 m/s (b) 4 m/s (c) 6 m/s (d) 8 m/s (e) 10 m/s

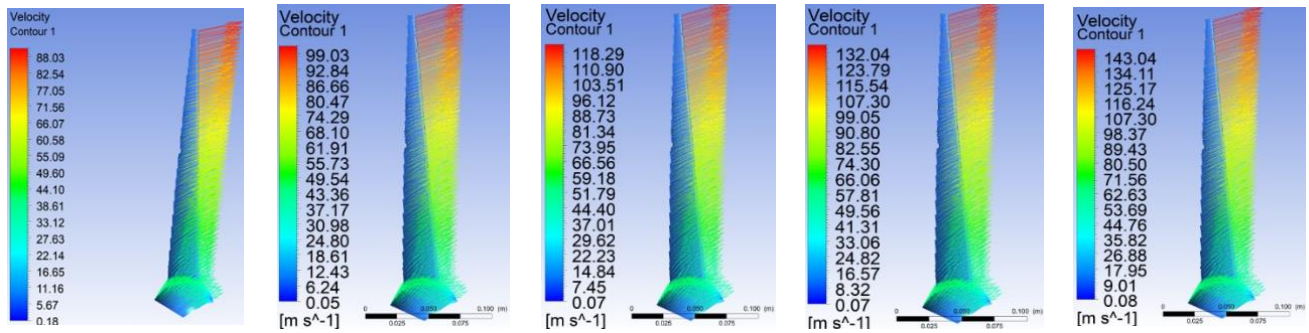

(f) 12 m/s (g) 14 m/s (h) 16 m/s (i) 18 m/s (j) 20 m/s

Fig.17.: Velocity contours over the suction side of the baseline blade for free stream velocities 1-20m/s obtained numerically

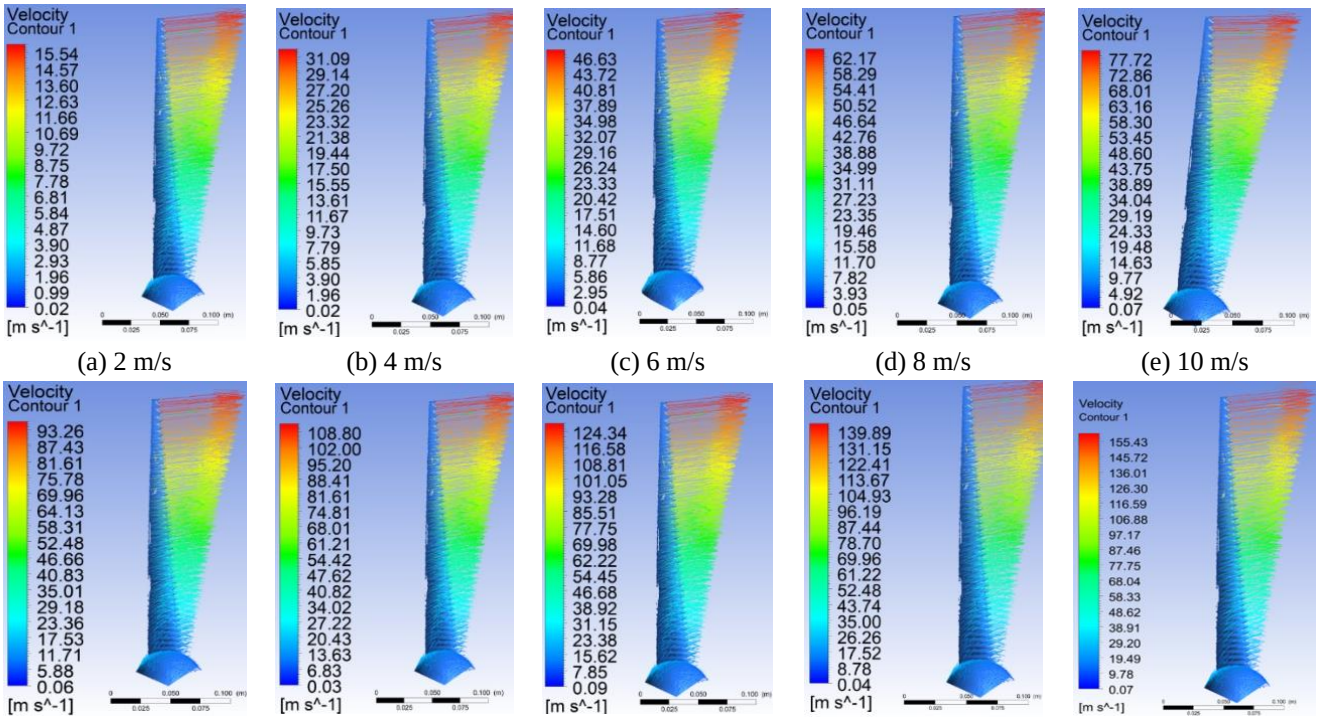

(a) 2 m/s (b) 4 m/s (c) 6 m/s (d) 8 m/s (e) 10 m/s

(f) 12 m/s (g) 14 m/s (h) 16 m/s (i) 18 m/s (j) 20 m/s

Fig.18. Velocity distribution for the modified blade tested for different wind velocities through ANSYS FLUENT

5.2 Discussion of Results

Figure 12 describes the analytical, numerical and experimental torque Q with respect to wind velocity U for the baseline and modified blades. Torque Q is one of the fundamental forces developed on the blade due to the relative motion between the blade and wind. The fluid-structure interaction establishes a pressure difference over the upper and lower surfaces of the blade that ultimately leads to the generation of aerodynamic forces and moments. Since the blades are free to rotate, the aerodynamic forces, specifically the lift force L will cause the blades to rotate with certain angular velocity Ω corresponding to a particular wind velocity U. The rotating blade will eventually cause the generator shaft to rotate and produce power. With increase in wind velocity, the pressure difference between the upper and lower blade surfaces intensifies and strengthens the aerodynamic lift, eventually improving the torque generated by the blades. Higher torque by the tubercled blade conveys that the blade is generating more lift and torque as compared to the baseline blade. This is true for both numerical and experimental cases. Modified blade with highest torque is regarded mainly to the presence of tubercles which was the only factor missing on the baseline blade. The torque outcome for the tubercled blade was very much in adherence to the outcomes of Weichao Shi et al [32], where the tubercled blades generated more torque as compared to the baseline blade.

To understand the substantial torque of the modified blade, the velocity vector plots presented in fig 17 and fig 18 for the baseline and modified blades can be considered. Closely observing and comparing the vector plots at all the

velocities, the modified blades displayed larger rotational velocities against the baseline blade at the same velocity. For instance, at 2m/s upwind velocity, the maximum velocity of the blade at the blade tip measured 13.75m/s whereas the modified blade exhibited a maximum tip velocity equal to 15.54m/s. The spike in velocity was around 13% more for the modified blade. Similarly, the modified blade showcased 4.5% of velocity improvement compared to the baseline blade at design velocity.

Various studies by authors have shown that the tubercle certainly aids in gently bending the incoming flow. As per Johari et al [39] the streamline flow, which was along the chordwise direction initially before encountering the tubercle, will bend outwards at each tubercle peak and then rolls downward along the either sides of the tubercle forming counter rotating vortices. These counter rotating vortices will roll down and eventually coalesce at the valleys of the tubercles leading to the reduction in pressure. The phenomenon occurring along the entire span of the blade will collectively cause the pressure along the suction side of the blade to further shrink. Unarguably, such phenomenon will yield in greater pressure differences and generally be large than the baseline blade. The same can be witnessed from the pressure contour plots of the baseline and modified blades as provided in fig 15 and fig 16. The average pressure difference on the suction side of the modified blade is visibly larger than the baseline blade. Large pressure differences naturally induce higher aerodynamic forces on the blade yielding faster angular velocity Ω and torque Q. The experimental torque trend for the baseline and modified blade displays remarkable performance improvements imparted by the tubercles that were actually not available from the simulation or theoretical outcomes.

Closer look at the experimental torque highlights the startup capabilities of both the blades. The first sign of blade rotation or blade startup was noted at 3.71m/s for baseline blade and 3.26m/s for the modified blade. Agreeably, it is understood that the modified blade cuts-in quickly because of which the useful torque is available much earlier than the baseline blade. In happening so, the tubercled blade functions substantially well even at low wind velocities or sub-optimal velocities which was otherwise an impossible task for the baseline blade. The encompassing feature subscribed by the modified blade convincingly proposes the tubercles to be capable of working even in low wind and also developing adequate torque to produce useful power. Surely this will be a crucial factor encouraging the widespread application of tubercled wind turbines in regions prone to low wind velocities affected by severe atmospheric boundary layer disturbances and also be instrumental in accomplishing commercial success. Again as the wind velocity incremented, the angular velocity Ω of the blade surged beyond the baseline blade capabilities and produced ample torque Q as seen from the figure 12.

The power characteristics of the baseline and modified blades were depicted in figure 13. Since, power P is a derived quantity from torque Q, the nature of power will be much similar to the torque behavior . It can be noticed that at 1 and 2m/s, the experimental power generated was zero for both baseline and modified blades which was not true for the BEM case where the blades were producing some finite amount of power despite velocities being so low. BEM method is just a far cry from actual reality. In the analytical evaluation, the blade performance parameters like torque, power etc. is determined under heavy assumptions. The BEM calculations also disregard the frictional losses between the blade and the moving wind, between the generator shaft and the bearings, hub losses and many more. As the theory neglects all the aforementioned losses, the BEMT will invariably produce power even when the velocity is just 1m/s that never occur in real working conditions.

Any wind turbine operating in open atmosphere, the blades will have certain inertia accounting to their self-weight. Besides, any generator will have an inherent cogging torque $Q_{Cogging}$ that will resist the rotation of the generator shaft because of the mechanical friction between the shaft and the coils. And also there will be serious friction between the shaft and the bearings. Wright et al [40] showed that, for easy start-up, the blades need to generate adequate torque to overcome the frictional, inertial forces, cogging torque of the motor failing to which the blades will be unable to rotate and generate any power. Generally, at low velocity, the momentum of the wind will be low to generate the required aerodynamic forces to develop useful torque. Resultantly, the blade torque Q will be unable to overcome the cogging torque of the generator, and hence do not generate any torque. For the present case, up to 3.71m/s and 3.26m/s for the baseline and modified blades respectively, there was no power generation. As the velocity surpasses 3.71m/s and 3.26m/s, the baseline and modified blades were obviously seen producing useful power. This vividly envisages the fact that at 3.71m/s and 3.26m/s, the baseline and modified blades have generated sufficient torque to completely overcome all the friction and cogging torque of the generator. Beyond these velocities, both the blades start to generate useful power output from the generator. Owing to these invariable consequences, the power developed during experiment would always be less.

At last, the representation of power output of the rotor blades in terms of coefficient of power C_P is provided in figure 14. Coefficient of power C_P is the ability of a rotor blade to extract kinetic energy from the wind to the total energy available in the wind. According to Betz, an ideal wind turbine

can only extract 59.26 % of energy from the wind irrespective of wind velocity. This concept is already reasoned and widely accepted as to why a wind turbine blade cannot extract all the available energy from the wind as stated by Haibo et al [41]. Betz limit is justifiable only for ideal and hypothetical situations. The drop in coefficient of power is much evident from figure 14 where the experimental C_P is marginally off the track with the BEM curves. As iterated in the previous section, under real operating conditions, the wind turbine blade endures a number of losses in the form of fluid and mechanical friction, drag losses, tip losses, transmission losses, generator losses and many more. Every wind turbine functioning in the open environment will inevitably experience the aforesaid losses and this is the reason for which the experimental C_P for the baseline and modified blades are always less than the BEM outcomes. Since, the power output of the baseline and modified blades achieved through BEM are high, even their corresponding power coefficient curves were greater than the experimental C_P. Nonetheless, the experimental C_P curves are deemed real and far more acceptable than the BEM behavior. The experimental behavior of the baseline model is in accordance with the experimental C_P outcome portrayed by Supreeth et al [42]. Additionally, the coefficient of power result obtained for the tubercled blade exhibiting both taper and twist are found to be performing satisfactorily. This can be compared with the outcomes of Guo-Yuan Huang et al [30] which portrayed the result of a tubercled blade without twist and taper. Despite considering the untapered and untwisted blade with different tubercle geometry, the power coefficient was around 0.30. In the current research work, the blades with taper and twist are seen to achieve more C_P in the same testing range showcasing the effect of taper and twist to be supporting the aerodynamic behavior of the blades. However, to derive better understanding about the contribution of tubercles, the blade performance needs to be ascertained at unsteady flow conditions which have not been accomplished in the future study.

Conclusions

The study involves significant efforts to improvise the performance of a 2kW small scale horizontal axis wind turbine for deploying in regions with sub-optimal wind velocities. To enhance the wind turbine performance in a cost effective manner, a passive flow control solution offered by the humpback whale tubercles was interspersed to the leading edge of the baseline wind turbine blade. The performances of the baseline as well as the tubercled wind turbine blade were independently introspected analytically, numerically and experimentally. From the extensive evaluation, critical information concerning wind turbine performance are highlighted as follows.

- At the outset of extensive investigation, the tubercled blade presented a distinctive performance that was appreciably superior to the baseline counterpart throughout testing range.

- Numerical simulation exhibited the modified blade with torque, power and coefficient of power to be greater by at least 24%, 26% and 7% compared to the baseline blade at the same tested conditions.

- In actual experimental testing, the presence of tubercles was much helpful in reducing the start-up or the cut-in velocity of modified blade by nearly 14%, which is a prominent contribution by the tubercles. This is of particular importance for wind turbines working in regions with low wind distribution or regions affected by atmospheric boundary layer.

- Finally, the evaluation of the blades highlights the benefits of embodying the simple humpback whale tubercles as passive flow control solution for improvising the performances of a small scale horizontal axis wind turbine in a cost effective manner.

Undoubtedly, the investigation has clearly concluded the incorporation of tubercles to surely impart better performance to the wind turbine blades. As a future task, the performance of the full scale wind turbine with tubercled blades would be appraised in an open unbounded domain to understand the true role of tubercles.

References

[1] Niu S, Jia Y, Wang W, He R, Hu L, Liu Y (2013). Electricity consumption and human development level: A comparative analysis based on panel data for 50 countries. International Journal of Electrical Power & Energy Systems.53:338–347.

[2] Administration UEI, et al.(2011) Annual Energy Outlook 2011: With Projections to 2035. Government Printing Office. Washington, DC, USA.

[3] Capuano L. International energy outlook 2018 (2018). US Energy Information Administration (EIA): Washington, DC, USA 2018;2018:21.

[4] Bank W. Tracking SDG 7: The energy progress report (2018), International Bank for Reconstruction and Development / The World Bank.

[5] Hasan, Md Mehedi (2017). Design and Performance Analysis of Small Scale Horizontal Axis Wind Turbine for Nano Grid Application, Electronic Theses & Dissertations. Georgia Southern University

[6] Sara Louise Walker (2011). Building mounted wind turbines and their suitability for the urban scale—A review

of methods of estimating urban wind resource, Energy and Buildings. 43-1852–1862

[7] Abdulkadir Mohamed Ali, "Aerodynamic Optimization of Small Scale Horizontal Axis Wind Turbine Blades", Masters Thesis, RMIT University, Melbourne, Australia

[8] Michael James Duffy, "Small Wind Turbines Mounted to Existing Structures" Masters Thesis, Georgia Institute of Technology

[9] Haseeb Shah, Sathyajith Mathew and Chee Ming Lim, "A Novel Low Reynolds Number Airfoil Design for Small Horizontal Axis Wind Turbines", Wind Engineering Volume 38, No. 4, 2014, PP 377–392

[10] Ravi Anant Kishore, Small-scale Wind Energy Portable Turbine (SWEPT), Master of Science Thesis, Virginia Polytechnic Institute and State University.

[11]Margrét Ósk Óskarsdóttir, "A General Description and Comparison of Horizontal Axis Wind Turbines and Vertical Axis Wind Turbines", ECTS thesis, Faculty of Industrial Engineering, Mechanical Engineering and Computer Science School of Engineering and Natural Sciences University of Iceland.

[12] Deibanehbok Nongdhar1 , Bikramjit Goswami, "Design of Micro Wind Turbine for Low Wind Speed Areas: A Review", ADBU Journal of Electrical and Electronics Engineering (AJEEE), Volume 2, Issue 1.

[13] Vaughn Nelson, "Wind Energy Renewable Energy and the Environment", Taylor & Francis Group, LLC, 2009, ISBN 978-1-4200-7568.

[14] Wind Power, Renewable Energy Technologies: Cost Analysis Series, Volume 1: Power Sector, Issue 5/5, June 2012.

[15] Fish, F. E. and Battle, J. M. (1995). Hydrodynamic design of the humpback whale flipper, J. Morphol. 225, 51-60.

[16] Bharat Bhushan, (2009). Biomimetics: lessons from nature – an overview. Phil. Trans. R. Soc. A. 367, 1445–1486.

[17] Y. Bar-Cohen, (2006). Biomimetics: biologically inspired technologies. Boca Raton, FL: Taylor & Francis.

[18] F. E. Fish, (2006). Limits of nature and advances of technology in marine systems: what does biomimetics have to offer to aquatic robots? Appl Bionics Biomech 3:49–60.

[19] I. Ibrahim, & T. H. New, (2015). Tubercle modifications in marine propeller blades.

[20] P. Watts, and F. E. Fish, (2001). The Influence of Passive, Leading Edge Tubercles on Wing Performance. Proceedings of the Twelfth International Symposium on Unmanned Untethered Submersible Technology (UUST), Autonomous Undersea Systems Inst., Lee, NH.

[21] K. L. Hansen, R. M. Kelso and B. B. Dally. (2009). The effect of leading edge tubercle Geometry on the performance of Different airfoils. ExHFT-7, 28 June – 03 July 2009, Krakow, Poland.

[22] Abdel Gawad, Ahmed. (2013). Utilization of Whale-Inspired Tubercles as a Control Technique to Improve Airfoil Performance. Transaction on Control and Mechanical Systems (TCMS). 2.

[23] Keerthi, M. C. et al. "Effect of Leading-Edge Tubercles on Compressor Cascade Performance." AIAA Journal 54 (2016): 912-923.

[24] Mishra, Alok & De, Ashoke. (2021). Investigation of passive flow control over an airfoil using leading edge tubercles.

[25] Arrondeau, Benjamin & Rana, Zeeshan. (2020). Computational Aerodynamics Analysis of Non-Symmetric Multi-Element Wing in Ground Effect with Humpback Whale Flipper Tubercles. Fluids. 5. 247. 10.3390/fluids5040247.

[26] N. Rostamzadeh, R. M. Kelso, B. B. Dally, and K. L. Hansen. (2013). The effect of undulating leading-edge modifications on NACA 0021 airfoil characteristics. Physics of Fluids. 25, 117101.

[27] Miklosovic, D. S., Murray, M. M., Howle, L. E. and Fish, F. E. (2014). Leading-edge tubercles delay stalls on humpback whale (Megaptera novaeangliae) flippers. Phys. Fluids. 16, L39-L42.

[28] R. Supreeth, A. Arokkiaswamy, K. Anirudh, R. K. Pradyumna, P. K. Pramod and A. K. Sanarahamat, (2020), Experimental and Numerical Investigation of the Influence of Leading Edge Tubercles on S823 Airfoil Behavior, Journal of Applied Fluid Mechanics, Vol. 13, No. 6, pp. 1885-1899, 2020, 10.47176/jafm.13.06.31244.[

[29] S. Arunvinthan, S. Nadaraja Pillai, Shuyang Cao. (2020). Aerodynamic characteristics of variously modified leading-edge protuberanced (LEP) wind turbine blades under various turbulent intensities, Journal of Wind Engineering & Industrial Aerodynamics 202 104188, doi.org/10.1016/j.jweia.2020.104188.

[30] Guo-Yuan Huang, Y.C.Shiah, Chi-Jeng Bai, W.T.Chong. (2015). Experimental study of the protuberance effect on the blade performance of a small horizontal axis wind turbine, J. Wind Eng.Ind.Aerodyn.147-202–211.

[31] Chang-Chi Huang, Chi-Jeng Bai, Y.C. Shiah, Yu-Jen Chen. (2016). Optimal design of protuberant blades for small variable-speed horizontal axis wind turbine-experiments and simulations, Energy. 115 1156-1167.

[32] Weichao Shi, Mehmet Atlar, Rosemary Norman. (2017). Detailed flow measurement of the field around tidal turbines with and without biomimetic leading-edge tubercles. Renewable Energy. 111, 688-707.

[33]J. Manwell, A. L. Rogers and J. G. McGowan. (2009). Wind Energy Explained Theory, Design and Application, 2nd ed., Chichester, West Sussex: John Wiley & Sons, Ltd.,

[34] Li, Guojie & Zhi, Jing. (2016). Analysis of Wind Power Characteristics. 10.1016/B978-0-12-849895-8.00002-6.

[35] Kishore, Ravi & Marin, Anthony & Priya, S.Jeba. (2014). Efficient Direct-Drive Small-Scale Low-Speed Wind Turbine. Energy Harvesting and Systems. 1. 10.1515/ehs-2014-0004.

[36] M. Berger, Cut cells: Meshes and solvers. In: Handbook of Numerical Analysis, vol. 18 Elsevier; 2017.p. 1–22.

[37] W. Hugh, W. Coleman, Jr. Glenn Steele, (12 February 1999). Experimentation, Validation, and Uncertainty Analysis for Engineers, Third Edition, John Wiley & Sons; 2nd edition.

[38] M. Bastankhah, F. Porté-Agel, (2017). A New Miniature Wind Turbine for Wind Tunnel Experiments. Part I: Design and Performance. Energies, 10, 908.

[39] H. Johari, C. Henoch, D. Custodio, and A. Levshin, (2007). Effects of leading edge protuberances on airfoil performance. AIAA J, 45, 2634.

[40] A.K. Wright, D.H. Wood. (2004). The starting and low wind speed behaviour of a small horizontal axis wind turbine, Journal of Wind Engineering and Industrial Aerodynamics 92-1265–1279.

[41] Haibo Jiang, Yanru Li, Zhongqing Cheng. (2015). Performances of ideal wind turbine. Renewable Energy 83 66-76.

[42] R. Supreeth, A. Arokkiaswamy, Nagarjun J. Raikar, H. P. Prajwal. (December, 2019). Experimental Investigation of Performance of a Small Scale Horizontal Axis Wind Turbine Rotor Blade, International Journal of Renewable Energy Research, Vol.9, No.4